

Superconductivity in 5.0° twisted bilayer WSe₂

<https://doi.org/10.1038/s41586-024-08381-1>

Received: 5 June 2024

Accepted: 8 November 2024

Published online: 22 January 2025

 Check for updates

Yinjie Guo¹, Jordan Pack¹, Joshua Swann¹, Luke Holtzman², Matthew Cothrine³, Kenji Watanabe⁴, Takashi Taniguchi⁵, David G. Mandrus^{3,6}, Katayun Barmak², James Hone⁷, Andrew J. Millis^{1,8}, Abhay Pasupathy^{1,9} & Cory R. Dean^{1✉}

The discovery of superconductivity in twisted bilayer and trilayer graphene^{1–5} has generated tremendous interest. The key feature of these systems is an interplay between interlayer coupling and a moiré superlattice that gives rise to low-energy flat bands with strong correlations⁶. Flat bands can also be induced by moiré patterns in lattice-mismatched and/or twisted heterostructures of other two-dimensional materials, such as transition metal dichalcogenides (TMDs)^{7,8}. Although a wide range of correlated phenomena have indeed been observed in moiré TMDs^{9–19}, robust demonstration of superconductivity has remained absent⁹. Here we report superconductivity in 5.0° twisted bilayer WSe₂ with a maximum critical temperature of 426 mK. The superconducting state appears in a limited region of displacement field and density that is adjacent to a metallic state with a Fermi surface reconstruction believed to arise from AFM order²⁰. A sharp boundary is observed between the superconducting and magnetic phases at low temperature, reminiscent of spin fluctuation-mediated superconductivity²¹. Our results establish that moiré flat-band superconductivity extends beyond graphene structures. Material properties that are absent in graphene but intrinsic among TMDs, such as a native band gap, large spin–orbit coupling, spin-valley locking and magnetism, offer the possibility of accessing a broader superconducting parameter space than graphene-only structures.

Flat bands in two-dimensional heterostructures have been a focus of intense study as a way to achieve strongly correlated electronic states. In twisted graphene systems, superconductivity^{1,2,4,5}, magnetic ordering²² and topological Chern bands²³ have been observed around commensurate fillings of the moiré band. Superconductivity has also been observed in crystalline graphene, such as rhombohedral trilayer graphene²⁴ and Bernal bilayer graphene^{25–27}, in which a high density of states is generated at Van Hove singularities (VHs), located at the boundary of Fermi pocket topology transitions.

Moiré-patterned transition metal dichalcogenides (TMDs) also host low-energy flat bands⁷ and have proven to be a highly tunable system for hosting exotic correlated phases, including Mott insulators^{9,10}, generalized Wigner crystal states^{12–14}, integer and fractional quantum anomalous Hall states^{15–19} and magnetic ordering¹¹. Theoretical studies have suggested that superconductivity should also be present in this system^{28–34}, with the possibility of exotic character. However, definitive experimental observation remains absent. This raises the question as to whether superconductivity is a universal feature in flat-band, two-dimensional systems, or whether there is some unique feature in graphene-based structures that plays a key role.

Here we report observation of superconductivity in bilayer WSe₂ fabricated with a 5.0° twist angle. At zero displacement field we do

not observe evidence of correlated behaviour; however, when an applied displacement field is tuned such that the VHs of the moiré band shift close to half filling (one hole per moiré unit cell), a local region of robust superconductivity emerges adjacent to a resistive metallic state that we associate with antiferromagnetic (AFM) ordering²⁰. Analysis of the superconductivity–AFM phase diagram suggests that superconductivity may be stabilized by spin fluctuations, analogous to similar behaviour seen in heavy fermion systems²¹.

Tunable flat bands

Figure 1a,b shows a schematic illustration of the device structure. The device reported here is an AA-stacked, twisted bilayer WSe₂ (tWSe₂) with twist angle measured to be 5.0° (Supplementary Fig. 2) Ohmic contacts were realized using a combination of graphite as the contact metal and RuCl₃ as a charge-transfer dopant in the contact region³⁵. We defined a three-gate structure in which ‘top’ and ‘bottom’ graphite gates allow tuning of both channel density and displacement field, with a third metal gate used to maintain a low electrostatic barrier in the contact region (see Methods for device structure and fabrication process). Contact resistance, estimated from the two-terminal response,

¹Department of Physics, Columbia University, New York, NY, USA. ²Department of Applied Physics and Applied Mathematics, Columbia University, New York, NY, USA. ³Department of Materials Science and Engineering, University of Tennessee, Knoxville, TN, USA. ⁴Research Center for Electronic and Optical Materials, National Institute for Materials Science, Tsukuba, Japan. ⁵Research Center for Materials Nanoarchitectonics, National Institute for Materials Science, Tsukuba, Japan. ⁶Materials Science and Technology Division, Oak Ridge National Laboratory, Oak Ridge, TN, USA. ⁷Department of Mechanical Engineering, Columbia University, New York, NY, USA. ⁸Center for Computational Quantum Physics, Flatiron Institute, New York, NY, USA. ⁹Condensed Matter Physics and Materials Science Division, Brookhaven National Laboratory, Upton, NY, USA. ✉e-mail: cd2478@columbia.edu

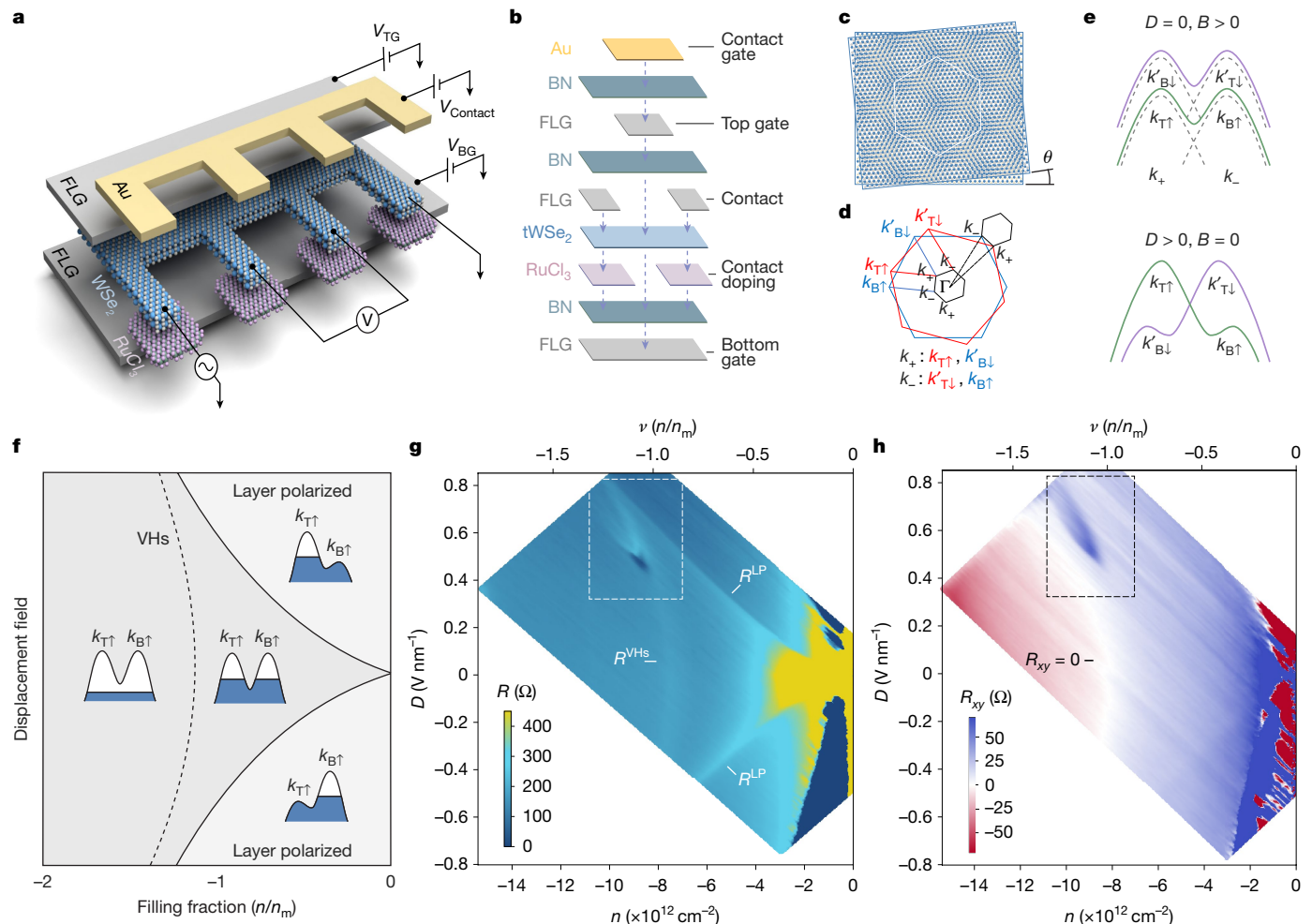


Fig. 1 | Electronic band structure and the superconducting pocket.

a,b, Schematic illustration of the tWSe₂ device structure showing the geometry (**a**) and layer sequence (**b**). Graphite contacts, together with charge-transfer doping by α -RuCl₃, enable ohmic contact. **c**, Illustration of the real-space moiré pattern between tWSe₂ layers; the device has a twist angle of 5.0°. **d**, Brillouin zones of the top (red) and bottom (blue) layers. Spin states near the k valleys are marked. The small black hexagon denotes the moiré mini-Brillouin zone. Both the spin-up (down) valley of the top layer and the spin-down (up) valley of the bottom layer fold onto the k_+ (k_-) valley of the moiré mini-Brillouin zone. $k_{T\uparrow}$ ($k'_{T\downarrow}$), spin-up (down) valley of the top layer; $k_{B\uparrow}$ ($k'_{B\downarrow}$), spin-up (down) valley of the bottom layer; k_+ , k_- , valleys of the moiré superlattice. **e**, Illustration of the low-energy tWSe₂ band structure. Spin-valley branches hybridize across the

layers as shown. The magnetic field splits the bands by Zeeman coupling (top), whereas the displacement field distorts each band by layer polarization. D , displacement field; B , magnetic field. **f**, A schematic phase diagram of the band structure and Fermi energy for a single isospin branch versus the displacement field and carrier density. The effective low-energy band structure for one of the isospin flavours is shown in each region. **g,h**, The longitudinal resistance, R (**g**), at zero magnetic field and Hall resistance, R_{xy} (**h**), at 200 mT, versus density and displacement field. Densities are shown as negative values to represent hole doping. Labels identify transport features that coincide with the solid and dashed boundaries in **f**. The filling fraction is defined as the number of holes per moiré unit cell. V_{TG} , top gate voltage; $V_{Contact}$, contact gate voltage; V_{BG} , bottom gate voltage; FLG, few-layer graphene.

is approximately 12 k Ω for most of the gate range, rising to 50 k Ω at a density of $0.95 \times 10^{12} \text{ cm}^{-2}$ (Supplementary Fig. 9).

In tWSe₂, lattice orientation mismatch of the rotated layers results in a moiré superlattice in real space, with moiré wavelength given by $\lambda = a/\sqrt{2(1 - \cos(\theta))}$ (ref. 36), where $a = 0.328 \text{ nm}$ for the lattice constant of monolayer WSe₂ and θ is the relative twist angle (Fig. 1c). At a twist angle of 5.0°, the moiré wavelength is 3.76 nm. In reciprocal space, a corresponding moiré mini-Brillouin zone is formed (Fig. 1d). The k_{\uparrow} (k'_{\downarrow}) valley of the top layer and the k'_{\downarrow} (k_{\uparrow}) valley of the down layer in the original Brillouin zone both fold onto the k_+ (k_-) valley in the moiré mini-Brillouin zone. Therefore, each valley of the moiré superlattice contains both spin flavours.

At small twist angles, interlayer hopping causes hybridization between layer bands, leaving a saddle point where they intersect (Fig. 1e). The reconstructed bands maintain spin and valley locking from the monolayer, and thus retain a twofold combined isospin flavour. Band structure calculations⁹ show that, at 5.0° twist angle, the ratio

of Coulomb energy U and bandwidth w is approximately 1, indicating a regime of moderate correlations. Application of a displacement field distorts each band, varying its width and causing the VHs position to shift and increase density of states at the VHs (Supplementary Fig. 7)⁹. At sufficiently large bias and low doping, the displacement field can cause the carriers to polarize to one layer. A cartoon schematic of the VHs position and layer polarization boundaries, as a function of displacement field and band filling, is shown in Fig. 1f.

Figure 1g shows longitudinal resistance, R , as a function of density and displacement field, measured at $B = 0 \text{ T}$ and cryostat temperature of $T = 33 \text{ mK}$. The conversion from applied gate potentials to density, displacement field and band filling fraction was determined from Landau level trajectories (Supplementary Fig. 2). We define filling fraction as the number of holes per moiré unit cell, $\nu = n/n_m$, where full band filling corresponds to $\nu = 2$ owing to the twofold isospin degeneracy. Both layer polarization boundaries and VHs position are evident, appearing as local peaks in R (light blue trajectories in Fig. 1g). Layer polarization

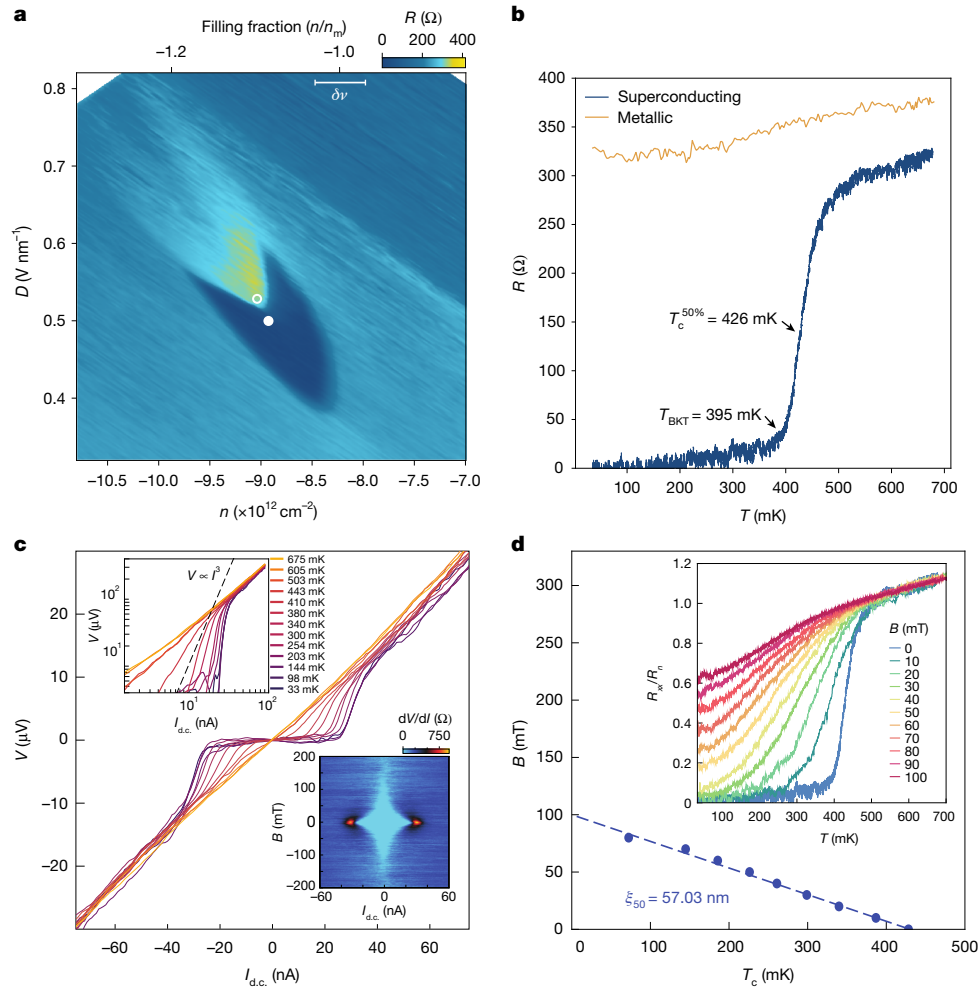


Fig. 2 | Superconductivity in tWSe₂. **a**, High-resolution map of the region enclosed by the dashed box in Fig. 1g, showing R around the superconducting pocket. The error bar shows the uncertainty in our determination of filling fraction (see Supplementary Fig. 2). The closed circle corresponds to $D = 0.53 \text{ V nm}^{-1}$, $n = -8.93 \times 10^{12} \text{ cm}^{-2}$; the open circle corresponds to $D = 0.53 \text{ V nm}^{-1}$, $n = -9.05 \times 10^{12} \text{ cm}^{-2}$. **b**, Resistance versus temperature measured at the locations identified in **a**. The critical temperature defined at 50% of the normal-state resistance ($T_c^{50\%}$) and the BKT temperature, T_{BKT} , determined in **c**, are labelled. **c**, V_{xx} – I as a function of temperature for the

zero-resistance location identified in **a**. The top left inset shows V_{xx} – I curves on a log–log scale. The dashed line indicates where the slope is 3 ($V_{xx} \propto I^3$), which gives $T_{\text{BKT}} = 395 \text{ mK}$. The bottom right inset shows dV_{xx}/dI versus direct current ($I_{\text{d.c.}}$) bias and perpendicular magnetic field. **d**, Critical temperature as a function of perpendicular magnetic field. The critical temperature is defined at 50% of the normal-state resistance from the family of $R(T)$ curves versus magnetic field, as shown in the inset. The error for T_c in all figures is around 10 mK, which is comparable to the size of the dots. ξ_{50} , coherence length extracted from T_c defined at 50% of the normal-state resistance.

boundaries, labelled R^{LP} in Fig. 1g, were confirmed by measurement in the quantum Hall regime, in which there is a corresponding change in Landau level crossing behaviour (Supplementary Fig. 1). The behaviour of the resistive peak at the approximate VHS position, labelled R^{VHS} in Fig. 1g, is a consequence of change in Fermi surface topology while doping across the VHS. Figure 1h shows the density and displacement field dependence of Hall resistance, R_{xy} , measured at $B = 0.2 \text{ T}$. R_{xy} changes sign along a similar trajectory (labelled $R_{xy} = 0$) as the R^{VHS} peak, but with a slight offset.

The temperature dependence of resistivity indicates that the material is metallic at all doping levels and displacement fields (Supplementary Fig. 12 shows temperature-dependent measurements). Under finite displacement field, approximately when the VHS exceeds half filling (dashed boxes in Fig. 1g,h), R demonstrates a local peak adjacent to a zero-resistance pocket whereas R_{xy} shows strong enhancement.

Superconductivity in tWSe₂

Figure 2a shows a higher-resolution map of the region enclosed by the dashed box in Fig. 1g, highlighting the zero-resistance region (dark blue

in the chosen colour scale). In Fig. 2b, temperature-dependent resistance at a select point in this region (solid circle in Fig. 2a) is compared with the adjacent resistive peak (open circle in Fig. 2a). The transition to zero resistance shows the characteristic behaviour of a two-dimensional superconductor: with decreasing temperature, resistance exhibits an abrupt downturn followed by a long tail that eventually reaches zero within the measurement noise floor. By comparison, the adjacent resistive peak exhibits a metallic dependence that is approximately linear in T . Using the empirical convention of identifying mean field critical temperature (T_c) to be that at which $R(T)$ equals 50% of normal-state resistance, $T_c = 426 \text{ mK}$ at this density and displacement field.

Figure 2c shows the temperature-dependent voltage–current (V – I) response for this same point. In the low-temperature limit, a nonlinear response typical of superconductivity is observed. We estimate the critical current at base temperature to be approximately $I_c = 30 \text{ nA}$. By fitting the power-law dependence (Fig. 2c, left inset), we extract a Berezinskii–Kosterlitz–Thouless (BKT) transition temperature of $T_{\text{BKT}} = 395 \pm 10 \text{ mK}$ (Methods and Supplementary Fig. 10), which is close to the estimated mean field temperature ($T_{\text{BKT}}/T_c = 0.93$), as expected for a low-disorder superconductor³⁷. The right-hand inset in Fig. 2c is a

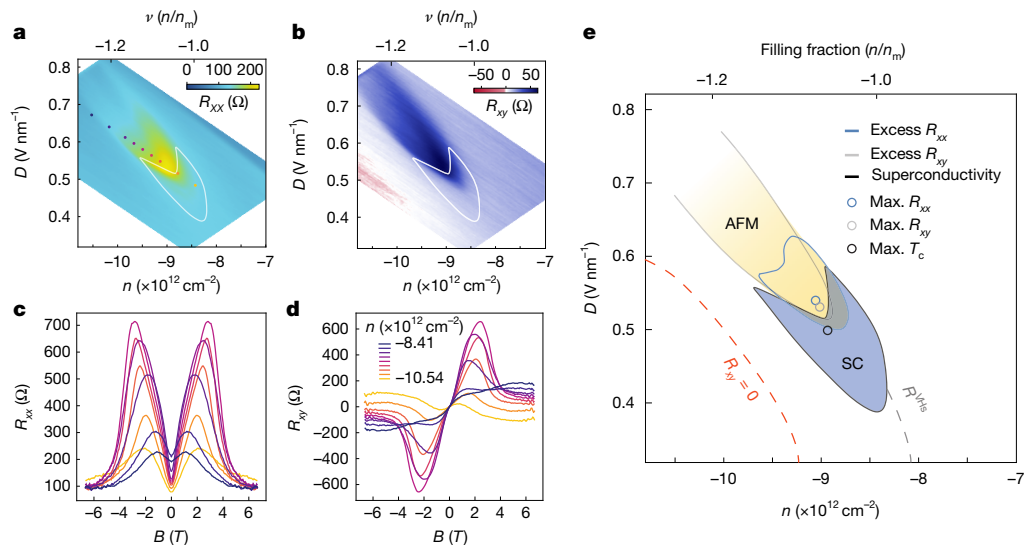


Fig. 3 | Magnetism and phase diagram. a,b, Longitudinal resistance (a) and Hall resistance (b), as a function of density and displacement field, measured at 200 mT, $T = 33$ mK. A resistive region is seen adjacent to, and overlapping with, the superconducting phase boundary (indicated by white line). **c,d**, Longitudinal resistance (c) and Hall resistance (d) versus magnetic field, measured at locations indicated by the coloured circles in **a**; $T = 1.6$ K. The legend in **d** identifies the corresponding densities. Anomalous magnetotransport is

plot of dV/dI versus direct current $I_{d.c.}$ and magnetic field. The qualitative behaviour is again consistent with superconductivity, and indicates a base temperature critical field of $B_{c\perp} \approx 100$ mT. If we assume a g factor of 20 (ref. 20), the Pauli limit is 250 mT.

Figure 2d shows the B – T phase diagram, determined using the same 50% R_n definition for T_c (a family of normalized $R(T)/R_n$ versus B curves is shown in the inset of Fig. 2d), in which normal-state resistance was defined by the knee of the transition. Critical temperature varies linearly with field, consistent with the Ginzburg–Landau equation, $B_{c2} = \phi_0 / (2\pi\xi(0)^2) (1 - (T/T_c))$, where ϕ_0 is the flux quantum, T_c is the zero field critical temperature and $\xi(0)$ is the coherence length. The slope of the fitted line gives $\xi(0) \approx 57$ nm. The normal-state square resistance, defined at the knee of the transition, is $R = 150 \Omega$. The mean free path, l_m , can be estimated from the Drude model, $R = h/e^2 k_F l_m$, where h is Planck's constant, e is elementary charge and $k_F = \sqrt{2\pi n}$, giving $l_m = 229$ nm. The disorder ratio is $d = \xi(0)/l_m \approx 0.25$, suggesting that the superconductor is in the clean limit.

Interplay between superconductivity and magnetic order

To further examine the resistive feature adjacent to the superconducting phase, we suppress the superconductor by applying an out-of-plane magnetic field. Figure 3a,b shows R_{xx} and R_{xy} measured at $B_{\perp} = 200$ mT, with the white line indicating the boundary of the superconducting pocket at zero field. In both channels we observe an excess resistance over a finite range of density and displacement field. Interestingly, the boundaries of the resistive and superconductor features occupy predominately separate regions, with a small overlap.

Figure 3c,d shows R_{xx} and R_{xy} versus B_{\perp} , measured at 1.6 K along the locations indicated by circles in Fig. 3a. The magnetoresistance characteristics in our 5.0° device are very similar to those reported in recent studies on 4.2° tWSe₂ (ref. 20) (Supplementary Information 4 provides additional magnetic field-dependent measurements at 1.6 K, and Supplementary Information 5 shows temperature-dependent measurements; magnetoresistance characteristics at dilution fridge base temperature are shown in Supplementary Information 13).

identified with an AFM order (see text). **e**, Relationship between superconducting (SC) and magnetic regions in the density-displacement field phase space. The AFM phase boundary is identified by the region of excess longitudinal resistance observed in **a** and excess Hall resistance observed in **b**. Blue and grey circles mark locations of the maximum (max) value in the 200 mT R_{xx} and R_{xy} maps, respectively; maximum T_c position (Fig. 4) is labelled by the black circle.

The peak in Hall resistance and the noticeable, but less marked, peak in longitudinal resistance were interpreted as having arisen from a Fermi surface reconstruction, most probably due to AFM order induced by the large susceptibility occurring at wave vectors that connect the Van Hove points of the spin-up and -down Fermi surfaces. Although direct evidence for AFM order cannot be provided by transport measurement alone, the theoretical calculations suggest that tWSe₂ is characterized by a strongly repulsive on-site electron–electron interaction predicted to favour AFM order^{20,38}. We calculate the density of states and wave vector-dependent susceptibility at the VHS as a function of displacement field, using the highest energy band from ref. 39 (Supplementary Fig. 8). The magnitude of this susceptibility increases with increasing displacement field, but the Fermi surface becomes less nested. On the basis of this trend, we suggest that, above a critical displacement field, the Stoner criterion is satisfied, yielding magnetic order.

A summary schematic of the full AFM–superconductor phase diagram is shown in Fig. 3e. Yellow indicates the region of AFM ordering identified by contours of excess resistance in R_{xx} (blue line) and R_{xy} (grey line). The blue region represents the arrow-shaped superconducting pocket observed at base temperature (Fig. 2a). The grey and red dashed lines indicate the R_{xx} peak and $R_{xy} = 0$ trajectories, respectively, associated with VHS (Fig. 1g,h). The locations of maximal excess resistance in R_{xx} (blue circle) and R_{xy} (grey circle) are essentially coincident with each other, and are both adjacent to, but not apparently overlapping, the location of peak superconducting T_c (black circle; see Fig. 4 for further details). We note that the appearance of superconductivity near an interaction-driven phase transition in spin-valley ordering is phenomenologically similar to observations in graphene-based flat-band systems^{1,3–5,24–27,40}.

We next examine how the phase diagram evolves with temperature. Figure 4a shows plots of R versus displacement field and density, measured at temperatures of 300, 400 and 640 mK. As temperature increases, the boundary of the superconducting pocket (dark blue) gradually shrinks. At 640 mK we see only a region of excess resistance remaining (yellow in the colour scale), corresponding to the same phase identified when suppressing the superconductor with magnetic field (Fig. 3a). Figure 4b shows a contour plot of the superconducting

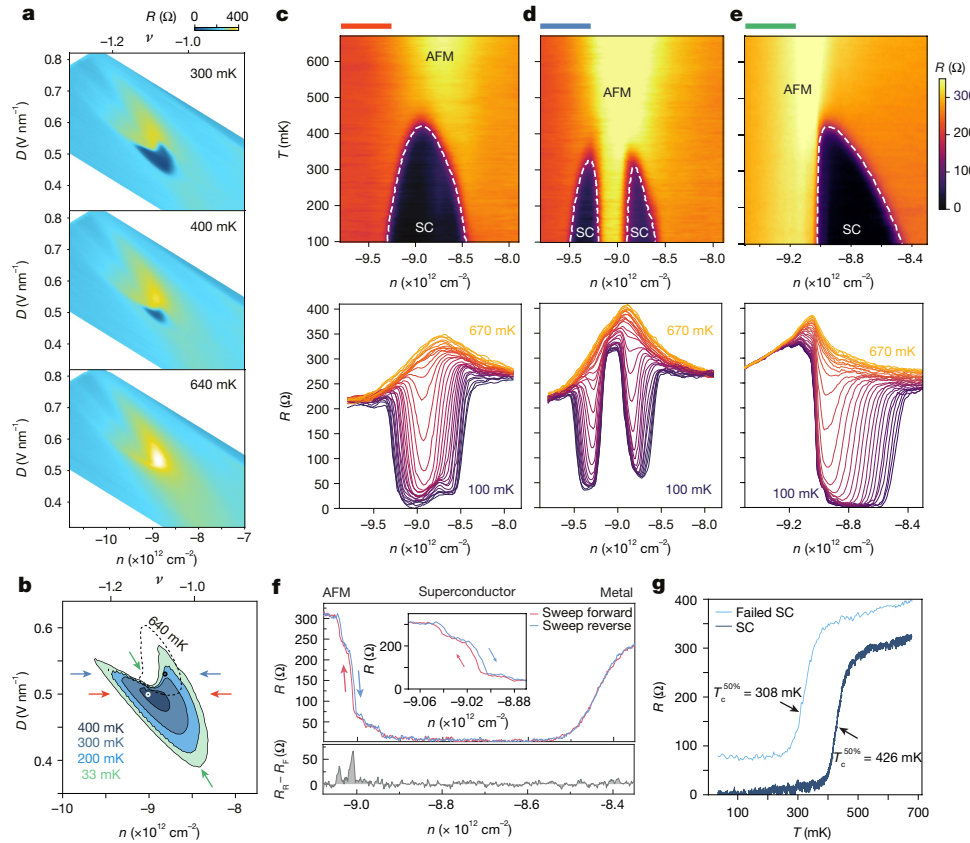


Fig. 4 | Temperature dependence of the superconducting boundary.

a, R versus displacement field and density measured at 300, 400 and 640 mK. As temperature exceeds T_c , only the region of excess resistance remains, which we associate with the AFM regime. **b**, Contour plot of the superconducting boundary versus temperature. The region of excess resistance measured at 640 mK is indicated by the dashed black line. **c–e**, Top, R plotted versus temperature and density, acquired by sweeping along line cuts in the D – n phase diagram. Coloured bars represent the associated trajectory marked by coloured arrows in **b**. Red (**c**) cuts across the superconducting region with largest T_c by varying density at fixed displacement field, $D = 0.50 \text{ V nm}^{-1}$;

blue (**d**) cuts across the strongest resistive peak, $D = 0.53 \text{ V nm}^{-1}$; green (**e**) cuts diagonally through both regions. Bottom, the associated family of curves. **f**, Top, forward (R_F) and reverse (R_R) traces along the trajectory measured in **e** showing evidence of hysteresis (emphasized inset) at the SC–AFM transition, but no hysteresis at the superconductivity–normal metal boundary. Bottom, difference between the traces. **g**, Comparison of $R(T)$ measured in the region of overlap between AFM and superconductivity boundaries (black circle in **b**), and outside the overlap region (white circle in **b**). The light blue curve, which is measured in the overlap region, shows the characteristics of a superconducting transition but saturates to a finite value before reaching zero resistance.

boundary at different temperatures (defined by 150Ω , about 50% of normal-state resistance). The dashed black line marks a contour boundary of excess resistance, corresponding to $R = 350 \Omega$ in the 640 mK map. As temperature increases, the boundary between the magnetic and superconducting phases remains sharp whereas the boundary furthest from the magnetic phase gradually recedes. This confirms that the region of most robust superconductivity is directly adjacent to the magnetic phase, but also shows that the phase transition between magnetic and superconducting states is sharply defined—possibly first order⁴¹.

Figure 4c–e shows cross-sections through the full temperature-displacement field-density phase space obtained by measurement of temperature dependence along the trajectories marked by coloured arrows in Fig. 4b. In each of these we get a sense of how the superconducting dome interplays with the surrounding phases. Figure 4c, obtained by varying density at fixed $D = 0.50 \text{ V nm}^{-1}$, cuts across the point of strongest T_c and intersects only the weak edge of the magnetic phase (red arrows in Fig. 4b). Although the corresponding superconducting dome boundary defined by T_c is approximately symmetric about the maximum T_c , at low temperature the line cuts show that resistance does not fully reach zero in the region of overlap with the magnetic phase. Figure 4d again corresponds to fixed D , but this time cutting across the region of strongest magnetic signature (blue arrows in Fig. 4b).

Here the apparent AFM state divides the dome in half, persisting all the way to base temperature. Finally, Fig. 4e cuts across the long diagonal pocket, intersecting the strongest superconductor and magnetic phase regions. Superconducting T_c shows a near-vertical drop to zero when it encounters the AFM phase boundary, but shows a more usual gradual dome-like shape when transitioning to the normal metal on the other side.

Figure 4f shows a single forward-and-reverse gate sweep measured along this same trajectory. We observe a weak hysteresis at the superconductivity–AFM transition, but no evidence of hysteresis across the superconductivity–metal transition under identical conditions. This provides further evidence of a first-order phase transition across the superconductivity–AFM boundary, and reinforces our interpretation that the Fermi surface reconstruction results from AFM ordering^{41–43}.

Finally, in Fig. 4g, we compare $R(T)$ between regions at which the superconductor and AFM overlap versus those at which they do not overlap, corresponding to the positions marked by the black and white circles, respectively, in Fig. 4b. In the overlapping region (light blue curve), $R(T)$ shows a sharp transition that closely resembles the non-overlapping region (dark blue curve), but with lower T_c . The transition in the overlap region does not reach zero resistance but instead saturates to a finite value. This behaviour suggests a failed

superconductor, which we conjecture arises from a mixed phase of AFM and superconducting regions.

Discussion and conclusions

Having demonstrated robust superconductivity in $tWSe_2$, we next consider what its nature might be. We first consider pairing strength. Estimation of Fermi energy (E_F) of about 50 meV (roughly half of full band width) gives the ratio for critical temperature, T_c , versus Fermi temperature ($T_F = E_F/k_B$) as $T_c/T_F \approx 0.0008$. This is a value typically associated with the weak-pairing Bardeen–Cooper–Schrieffer (BCS) regime⁴⁴. The BKT relation implies that, at $T = T_{BKT}$, superfluid stiffness, $\rho_s(T) = \frac{2}{\pi} T_c$, is approximately 0.25 K, much lower than the clean-limit superfluid stiffness of approximately 20 meV calculated from the band structure given in ref. 39. From the density at which the superconductivity dome exists, we estimate interparticle distance d to be around 3.33 nm. The ratio of coherence length to interparticle distance ($\xi(0)/d$) is therefore about 17, a relatively high value. The low value of superfluid stiffness, high value of coherence length relative to interparticle distance, and large band width all support BCS pairing.

It has been proposed theoretically that phonon-mediated interactions could induce a conventional type of superconductivity in graphene flat-band systems^{40,45,46}, with similar possibilities anticipated in $tWSe_2$ (refs. 7,29). Although we estimate that this system is within the BCS limit, we nonetheless conjecture that the superconductivity is unconventional in the sense of being induced by a non-phonon mechanism. A feature that distinguishes our system from twisted multilayer graphene systems^{1,3–5,40}, but that finds similarity with rhombohedral trilayer graphene²⁴ and Bernal bilayer graphene^{25–27}, is the emergence of superconductivity coincident with a Fermi surface reconstruction in which magnetic ordering in the spin-valley sector is also evident. In twisted graphene, there is ambiguity because the narrowness of the band makes it difficult to determine proximity relationships between the various ordered states⁴⁵. If the superconductivity in our device were phonon mediated with an enhancement by the Van Hove density of states, we might expect it to track the VHs throughout the band. The fact that, instead, we observe superconductivity only within a narrow window, concomitant with magnetic ordering, points towards magnetic order playing a critical role, such as mediation of pairing with spin fluctuation^{21,32,47,48}.

In summary, our interpretation is that, at zero displacement field, correlations are too weak for superconductivity to be observable within experimental temperature. However, under application of a displacement field, the resulting increase in density of states at the VHs and increasing magnetic susceptibility reach a threshold at which a Fermi surface reconstruction to an AFM state results. Spin fluctuations in the vicinity of the AFM phase are then responsible for mediating the superconducting pairing state. This interpretation would explain the absence of superconductivity everywhere, except in proximity to the AFM phase, while also being qualitatively consistent with the superconducting phase defined by T_c that rises approaching the AFM phase, reaches a peak value at the AFM boundary and then abruptly disappears. Finally, we note that this behaviour is very similar to AFM heavy fermion systems in the clean limit at which spin fluctuations provide the pairing mechanism^{21,49}.

A full understanding of the superconductivity, and the precise mechanism that we observe in $tWSe_2$, will certainly require further experimental and theoretical work. In particular, a more comprehensive understanding of the interplay between magnetic order and superconducting state, beyond what can be accomplished by transport alone, will be necessary to determine whether the two phases are cooperative, competing, coincident or some combination of all three. A key question to address will be how phase diagram evolves with twist angle. This also provides a unique opportunity compared with graphene systems, because it is already established that, in the TMDs, correlations

survive and evolve over several degrees of twist angle, compared with the relatively narrow ‘magic’ windows in twisted multilayer graphene, and the essentially singular parameter space of rhombohedral stacked multilayers.

During the preparation of this article, we became aware of similar studies on the observation of superconductivity in $3.65^\circ tWSe_2$ (ref. 50).

Online content

Any methods, additional references, Nature Portfolio reporting summaries, source data, extended data, supplementary information, acknowledgements, peer review information; details of author contributions and competing interests; and statements of data and code availability are available at <https://doi.org/10.1038/s41586-024-08381-1>.

- Cao, Y. et al. Unconventional superconductivity in magic-angle graphene superlattices. *Nature* **556**, 43–50 (2018).
- Yankowitz, M. et al. Tuning superconductivity in twisted bilayer graphene. *Science* **363**, 1059–1064 (2019).
- Lu, X. et al. Superconductors, orbital magnets and correlated states in magic-angle bilayer graphene. *Nature* **574**, 653–657 (2019).
- Park, J. M., Cao, Y., Watanabe, K., Taniguchi, T. & Jarillo-Herrero, P. Tunable strongly coupled superconductivity in magic-angle twisted trilayer graphene. *Nature* **590**, 249–255 (2021).
- Hao, Z. et al. Electric field-tunable superconductivity in alternating-twist magic-angle trilayer graphene. *Science* **371**, 1133–1138 (2021).
- Bistritzer, R. & MacDonald, A. H. Moiré bands in twisted double-layer graphene. *Proc. Natl Acad. Sci. USA* **108**, 12233–12237 (2011).
- Wu, F., Lovorn, T., Tutuc, E. & MacDonald, A. H. Hubbard model physics in transition metal dichalcogenide moiré bands. *Phys. Rev. Lett.* **121**, 026402 (2018).
- Naik, M. H. & Jain, M. Ultraflatbands and shear solitons in moiré patterns of twisted bilayer transition metal dichalcogenides. *Phys. Rev. Lett.* **121**, 266401 (2018).
- Wang, L. et al. Correlated electronic phases in twisted bilayer transition metal dichalcogenides. *Nat. Mater.* **19**, 861–866 (2020).
- Tang, Y. et al. Simulation of Hubbard model physics in WSe_2/WS_2 moiré superlattices. *Nature* **579**, 353–358 (2020).
- Anderson, E. et al. Programming correlated magnetic states via gate controlled moiré geometry. *Science* **381**, 325–330 (2023).
- Regan, E. C. et al. Mott and generalized Wigner crystal states in WSe_2/WS_2 moiré superlattices. *Nature* **579**, 359–363 (2020).
- Li, H. et al. Imaging two-dimensional generalized Wigner crystals. *Nature* **597**, 650–654 (2021).
- Xu, Y. et al. Correlated insulating states at fractional fillings of moiré superlattices. *Nature* **587**, 214–218 (2020).
- Li, T. et al. Quantum anomalous Hall effect from intertwined moiré bands. *Nature* **600**, 641–646 (2021).
- Cai, J. et al. Signatures of fractional quantum anomalous Hall states in twisted $MoTe_2$ bilayer. *Nature* **622**, 63–68 (2023).
- Zeng, Y. et al. Thermodynamic evidence of fractional Chern insulator in moiré $MoTe_2$. *Nature* **622**, 69–73 (2023).
- Park, H. et al. Observation of fractionally quantized anomalous Hall effect. *Nature* **622**, 74–79 (2023).
- Foutty, B. A. et al. Mapping twist-tuned multiband topology in bilayer WSe_2 . *Science* **384**, 343–347 (2024).
- Ghiotto, A. et al. Stoner instabilities and Ising excitonic states in twisted transition metal dichalcogenides. Preprint at <https://arxiv.org/abs/2405.17316> (2024).
- Mathur, N. D. et al. Magnetically mediated superconductivity in heavy fermion compounds. *Nature* **394**, 39–43 (1998).
- Sharpe, A. L. et al. Emergent ferromagnetism near three-quarters filling in twisted bilayer graphene. *Science* **365**, 605–608 (2019).
- Serlin, M. et al. Intrinsic quantized anomalous Hall effect in a moiré heterostructure. *Science* **367**, 900–903 (2020).
- Zhou, H., Xie, T., Taniguchi, T., Watanabe, K. & Young, A. F. Superconductivity in rhombohedral trilayer graphene. *Nature* **598**, 434–438 (2021).
- Zhou, H. et al. Isospin magnetism and spin-polarized superconductivity in Bernal bilayer graphene. *Science* **375**, 774–778 (2022).
- Zhang, Y. et al. Enhanced superconductivity in spin-orbit proximitized bilayer graphene. *Nature* **613**, 268–273 (2023).
- Li, C. et al. Tunable superconductivity in electron- and hole-doped Bernal bilayer graphene. *Nature* **631**, 300–306 (2024).
- Venderley, J. & Kim, E.-A. Density matrix renormalization group study of superconductivity in the triangular lattice Hubbard model. *Phys. Rev. B* **100**, 060506 (2019).
- Hsu, Y.-T., Wu, F. & Das Sarma, S. Spin-valley locked instabilities in moiré transition metal dichalcogenides with conventional and higher-order Van Hove singularities. *Phys. Rev. B* **104**, 195134 (2021).
- Schrade, C. & Fu, L. Nematic, chiral and topological superconductivity in transition metal dichalcogenides. *Phys. Rev. B* **110**, 035143 (2024).
- Crépeel, V., Guerci, D., Cano, J., Pixley, J. H. & Millis, A. Topological superconductivity in doped magnetic moiré semiconductors. *Phys. Rev. Lett.* **131**, 056001 (2023).
- Klebl, L., Fischer, A., Classen, L., Scherer, M. M. & Kennes, D. M. Competition of density waves and superconductivity in twisted tungsten diselenide. *Phys. Rev. Res.* **5**, L012034 (2023).

33. Zhou, B. & Zhang, Y.-H. Chiral and nodal superconductors in the t - J model with valley contrasting flux on a triangular moiré lattice. *Phys. Rev. B* **108**, 155111 (2023).
34. Zegrodnik, M. & Biborski, A. Mixed singlet-triplet superconducting state within the moiré t - J - U model applied to twisted bilayer WSe_2 . *Phys. Rev. B* **108**, 064506 (2023).
35. Pack, J. et al. Charge-transfer contacts for the measurement of correlated states in high-mobility WSe_2 . *Nat. Nanotechnol.* **19**, 948–954 (2024).
36. Yankowitz, M. et al. Emergence of superlattice Dirac points in graphene on hexagonal boron nitride. *Nat. Phys.* **8**, 382–386 (2012).
37. Beasley, M. R., Mooij, J. E. & Orlando, T. P. Possibility of vortex-antivortex pair dissociation in two-dimensional superconductors. *Phys. Rev. Lett.* **42**, 1165–1168 (1979).
38. Zang, J., Wang, J., Cano, J. & Millis, A. J. Hartree-Fock study of the moiré Hubbard model for twisted bilayer transition metal dichalcogenides. *Phys. Rev. B* **104**, 075150 (2021).
39. Crépel, V. & Millis, A. Bridging the small and large in twisted transition metal dichalcogenide homobilayers: A tight binding model capturing orbital interference and topology across a wide range of twist angles. *Phys. Rev. Res.* **6**, 033127 (2024).
40. Liu, X. et al. Tuning electron correlation in magic-angle twisted bilayer graphene using Coulomb screening. *Science* **371**, 1261–1265 (2021).
41. Holleis, L. et al. Nematicity and orbital depairing in superconducting Bernal bilayer graphene with strong spin orbit coupling. Preprint at <https://arxiv.org/abs/2303.00742> (2023).
42. Yang, Z., Lange, M., Volodin, A., Szymczak, R. & Moshchalkov, V. V. Domain-wall superconductivity in superconductor–ferromagnet hybrids. *Nat. Mater.* **3**, 793–798 (2004).
43. Mukherjee, A. et al. Superconducting magic-angle twisted trilayer graphene hosts competing magnetic order and moiré inhomogeneities. Preprint at <https://arxiv.org/abs/2406.02521> (2024).
44. Bardeen, J., Cooper, L. N. & Schrieffer, J. R. Theory of superconductivity. *Phys. Rev.* **108**, 1175–1204 (1957).
45. Balents, L., Dean, C. R., Efetov, D. K. & Young, A. F. Superconductivity and strong correlations in moiré flat bands. *Nat. Phys.* **16**, 725–733 (2020).
46. Wu, F., MacDonald, A. H. & Martin, I. Theory of phonon-mediated superconductivity in twisted bilayer graphene. *Phys. Rev. Lett.* **121**, 257001 (2018).
47. Fischer, A., Klebl, L., Honerkamp, C. & Kennes, D. M. Spin-fluctuation-induced pairing in twisted bilayer graphene. *Phys. Rev. B* **103**, L041103 (2021).
48. Zhai, H., Wang, F. & Lee, D.-H. Antiferromagnetically driven electronic correlations in iron pnictides and cuprates. *Phys. Rev. B* **80**, 064517 (2009).
49. Scalapino, D. J. A common thread: the pairing interaction for unconventional superconductors. *Rev. Mod. Phys.* **84**, 1383–1417 (2012).
50. Xia, Y. et al. Superconductivity in twisted bilayer WSe_2 . *Nature* <https://doi.org/10.1038/s41586-024-08116-2> (2024).

Publisher's note Springer Nature remains neutral with regard to jurisdictional claims in published maps and institutional affiliations.

Springer Nature or its licensor (e.g. a society or other partner) holds exclusive rights to this article under a publishing agreement with the author(s) or other rightsholder(s); author self-archiving of the accepted manuscript version of this article is solely governed by the terms of such publishing agreement and applicable law.

© The Author(s), under exclusive licence to Springer Nature Limited 2025

Methods

Device fabrication

Images for device stacking and fabrication are shown in Supplementary Fig. 11. We use a thin polycarbonate film to pick up the exfoliated layers from SiO₂ with the dry-transfer method⁵¹. We use thin boron nitride as the dielectric spacer to increase displacement field and density range in the phase diagram. Few-layer graphite are used for top and bottom gates. We use graphite with fewer layers as contacts for WSe₂ layers, and a thin RuCl₃ flake is stacked in the contact region to improve these contacts. The contact doping scheme^{39,52,53} enables reliable contact under hole doping only, and therefore we restrict our discussion to studies of the valence band. This device was assembled by the dry-transfer method⁵¹ using exfoliated hexagonal BN as dielectric spacers (Fig. 1b). The WSe₂ layers are derived from high-purity crystals grown by a two-step flux synthesis method⁵⁴. We stack the layers from top to bottom in the following sequence: topmost BN (about 11 nm), graphite top gate, top BN (around 5 nm), graphite contacts, twisted WSe₂ layers, α -RuCl₃ layer, bottom BN (roughly 17 nm) and graphite bottom gate. Particular care is taken in alignment of the graphite top gate, graphite contact and α -RuCl₃, to ensure that the top gate is local to the channel region, and to avoid overlapping with the contact region. The ‘cut-and-stack’ technique⁵⁵ was used to realize an AA-stacked tWSe₂. We precut a WSe₂ monolayer into two pieces with an atomic force microscope tip, then pick up one of the pieces and rotate the transfer stage by about 5.0° before picking up the second piece. Finally, we drop the stack onto a SiO₂ substrate.

A metal contact gate is deposited on top of the stack to smooth the gap between the heavily doped contact region by α -RuCl₃ and the intrinsic channel region. Metal leads to the gates and graphite contacts are deposited following etching through BN with the same polymethylmethacrylate mask. Finally, the device is etched into a Hall bar shape with alternating SF₆ and O₂ plasmas, with a 30 W O₂ plasma at the end to etch through the α -RuCl₃ flake. Polymethylmethacrylate is left on the chip following the etching process, to avoid any exposure of α -RuCl₃ to solvents. The device is stacked and fabricated in the same way as detailed in ref. 35.

Measurements

Transport measurements were performed in a variable temperature cryostat with a base temperature of 1.6 K, and in a dilution fridge with a base temperature of 33 mK. Four- and two-terminal resistance measurements were carried out using a low-frequency lock-in technique at frequencies ranging from 6 to 25 Hz. Characterization for the superconducting region was done with a current source bias of 5 nA. V - I characteristics were measured in direct current using a sourcemeter and nanovoltmeters. dV/dI measurements were carried out using lock-in SR860 to provide an alternating current signal in addition to the direct current signal. Current signal was amplified using a SR570 and measured with SR860s and a nanovoltmeter. Measurement configurations and characteristics of different lead combinations are shown in Supplementary Fig. 3. Supplementary Fig. 14 shows a schematic of the edges of α -RuCl₃ with respect to the region through which current follows.

Tunable bands in tWSe₂

In Fig. 1g, the diverging R seen at low density (yellow in the chosen colour scale) corresponds to Fermi level nearing the top of the valence band. The behaviour of the resistive peak, labelled R^{VHs} , is consistent with band structure calculations predicting that the VHs is located slightly below half-band filling at $D = 0$, and passes through half filling at approximately $D = 0.4 \text{ V nm}^{-1}$ (ref. 39 and Supplementary Fig. 7). The temperature dependence of resistivity indicates that the material is metallic at all doping levels and displacement

fields (Supplementary Fig. 12 shows temperature-dependent measurements), in contrast to previous studies of devices with smaller twist angles, which showed small regions of fully insulating (but modest band gap) behaviour^{9,20}. We attribute this difference to the larger twist angle (implying larger band width) and reduced BN thickness (implying potentially more screening by the gate).

BKT temperature extraction

We plot V_{xx} - I curves measured at different temperatures on a log-log scale (Fig. 2c, inset). We extract the power at different temperatures in the transition region. To determine the temperature at which the curve follows $V \propto I^{\beta}$, we plot power versus temperature and interpolate to find where it crosses 3 (Supplementary Fig. 10)

Theory

We used the formalism of ref. 39, which presents a three-band, tight-binding model with parameters fit to discrete Fourier transform calculations, for determination of band structure. Because this paper gives parameters for angles only up to 4.5°, we thus extrapolated to 5.0°. In the notation of ref. 39 we find (all energies in meV) $\delta = 15$, $t_1^{\text{th}} = 15$, $t_1^{\text{hh}} = 2$, $t_2^{\text{th}} = 0$, $t_1^{\text{tt}} = -2$, $t_3^{\text{hh}} = 4$, where t represents triangular, h represents honeycomb, and we considered displacement fields up to 18 meV. We computed band energy on a dense grid of k -points in the Brillouin zone (BZ), identified the highest-lying electron band ε_k^3 and then used these energies to construct the single-spin density of states $N_0(\omega) = \int_{\text{BZ}} \frac{d^2k}{(2\pi)^2} \delta(\omega - \varepsilon_k^3)$ and

both transverse $\chi^{\pm}(q, 0) = \mathcal{P} \int_{\text{BZ}} \frac{d^2k}{(2\pi)^2} \frac{f(\varepsilon_k^{3,\uparrow}) - f(\varepsilon_{k+q}^{3,\downarrow})}{\varepsilon_k^{3,\uparrow} - \varepsilon_{k+q}^{3,\downarrow}}$ and longitudinal $\chi^{\text{zz}}(q, 0) = \mathcal{P} \sum_{\sigma} \int_{\text{BZ}} \frac{d^2k}{(2\pi)^2} \frac{f(\varepsilon_k^{3,\sigma}) - f(\varepsilon_{k+q}^{3,\sigma})}{\varepsilon_k^{3,\sigma} - \varepsilon_{k+q}^{3,\sigma}}$ susceptibilities (\mathcal{P} denotes principal value). At this level of approximation there is no qualitative difference between longitudinal and transverse susceptibilities. Supplementary Fig. 7 shows the density of states for different displacement fields.

Data availability

The data relevant to figures in the main text are available via Zenodo at <https://doi.org/10.5281/zenodo.13910339> (ref. 56). Additional raw data are available from the corresponding author on reasonable request.

- Wang, L. et al. One-dimensional electrical contact to a two-dimensional material. *Science* **342**, 614–617 (2013).
- Sternbach, A. J. et al. Quenched excitons in WSe₂/ α -RuCl₃ heterostructures revealed by multimessenger nanoscopy. *Nano Lett.* **23**, 5070–5075 (2023).
- Xie, J. et al. Low resistance contact to P-type monolayer WSe₂. *Nano Lett.* **24**, 5937–5943 (2024).
- Liu, S. et al. Two-step flux synthesis of ultrapure transition-metal dichalcogenides. *ACS Nano* **17**, 16587–16596 (2023).
- Kim, K. et al. Van der Waals heterostructures with high accuracy rotational alignment. *Nano Lett.* **16**, 1989–1995 (2016).
- Guo, Y. Data related to “Superconductivity in 5.0° twisted bilayer WSe₂”. Zenodo <https://doi.org/10.5281/zenodo.13910339> (2024).

Acknowledgements This research on superconductivity in tWSe₂ structures is solely supported as part of Programmable Quantum Materials, an Energy Frontier Research Center funded by the US Department of Energy, Office of Science, Basic Energy Sciences, under award no. DE-SC0019443. WSe₂ was synthesized by J.H. and K.B. with the support of the Columbia University Materials Science and Engineering Research Center, through NSF grant no. DMR-2011738. D.G.M. and M.C. acknowledge support from the Gordon and Betty Moore Foundation’s EPIQS Initiative (grant no. GBMF9069). K.W. and T.T. acknowledge support from JSPS KAKENHI (grant nos. 21H05233 and 23H02052) and the World Premier International Research Center Initiative, MEXT, Japan. J.H. and C.R.D. acknowledge additional support from the Gordon and Betty Moore Foundation’s EPIQS Initiative (grant no. GBMF10277).

Author contributions Y.G. fabricated the device. Y.G., J.P., J.S. and C.R.D. performed electronic transport measurements and analysed data. L.H. grew WSe₂ crystals under the supervision of J.H. and K.B. M.C. grew α-RuCl₃ crystals under the supervision of D.G.M. K.W. and T.T. grew hexagonal boron nitride crystals. A.M. performed theoretical modelling. Y.G., A.J.M., A.P. and C.R.D. wrote the manuscript, with input from all authors.

Competing interests The authors declare no competing interests.

Additional information

Supplementary information The online version contains supplementary material available at <https://doi.org/10.1038/s41586-024-08381-1>.

Correspondence and requests for materials should be addressed to Cory R. Dean.

Peer review information *Nature* thanks Sergio de la Barrera, Zheng Zhu and the other, anonymous, reviewer(s) for their contribution to the peer review of this work.

Reprints and permissions information is available at <http://www.nature.com/reprints>.